Fossilization of Precambrian microfossils in the Volyn pegmatite, Ukraine

Gerhard Franz[1], Peter Lyckberg[2], Vladimir Khomenko[3], Vsevolod Chournousenko[4], Hans-Martin Schulz[5], Nicolaj Mahlstedt[5], Richard Wirth[5], Johannes Glodny[5], Uli Gernert[6], Jörg Nissen[6]

[1]Institut für Angewandte Geowissenschaften, Technische Universität Berlin, D-10587 Berlin, Germany

[2]Luxembourg National Museum of Natural History, 25 Rue Münster, 2160 Luxembourg, Luxembourg

[3]The National Academy of Sciences of Ukraine, M.P. Semenenko Institute of Geochemistry, Mineralogy and Ore Formation, 34, Palladina av., Kyiv, 03142, Ukraine

[4]Volyn Quartz Samotsvety Company, Khoroshiv (Volodarsk-Volynski), Ukraine

[5]GFZ German Research Centre for Geosciences, Telegrafenberg, D-14473 Potsdam, Germany

[6]Zentraleinrichtung Elektronenmikroskopie, Technische Universität Berlin, D-10623 Berlin, Germany

Corresponding author: Gerhard Franz; e-mail: gefra548@gmail.com

Abstract

We report on Precambrian microfossils from igneous rocks of the Volyn pegmatite district, associated with the Paleoproterozoic Korosten Pluton, north-western Ukraine. The fossils were recovered from m-sized miarolitic cavities and show a well-preserved 3D morphology, mostly filamentous, but with a large variety of types, and also in irregular, flaky shapes reminiscent of former biofilms, and rare spherical objects. Based on literature data, pyrolysis experiments and reflected light microscopy results, the organic matter (OM) is characterized as (oxy)kerite. Further investigations with microscopic techniques, including scanning and transmission electron microscopy, and electron microprobe analysis show that fossilization likely occurred during a hydrothermal, post-pegmatitic event, by silicification dominantly in the outermost 1-2 µm of the microfossils. The hydrothermal fluid, derived from the pegmatitic environment, was enriched in SiF_4, Al, Ca, Na, K, Cl, and S. The OM shows O enrichment where N and S content is low, indicating simultaneous N and S loss during anaerobic oxidation. Mineralization with Al-silicates starts at the rim of the microfossils, continues in its outer parts into identifiable encrustations and intergrowths of clay minerals, feldspar, Ca-sulfate, Ca-phosphate, Fe-sulfide, and fluorite.

Breccias, formed during collapse of some the miarolitic cavities, contain decaying OM, which released high concentrations of dissolved NH_4^+, responsible for the late-stage formation of buddingtonite and tobelite-rich muscovite. The age of the fossils can be restricted to the time between the pegmatite formation, at ~1.760 Ga, and the breccia formation at ~ 1.49 Ga. As geological environment for growth of the microorganisms and fossilization we assume a geyser system, in which the essential biological components C, N, S, and P for growth of the organisms in the miarolitic cavities were derived from microorganisms at the surface. Fossilization was induced by magmatic SiF_4-rich fluids. The Volyn occurrence is a distinct and uncommon

44   example of Precambrian fossils and the results underline the importance of cavities in granitic

45   rocks as a possible habitat for microorganisms preserved in the deep biosphere.

46

47   Key words: microfossils, fossilization, Precambrian, pegmatite, deep biosphere

1. Introduction

Precambrian fossils are rare and their morphology is generally not well preserved. They occur mostly in (meta)sedimentary rocks, but in recent years it became evident that pores, fissures and other open spaces in igneous rocks can be a habitat for microorganisms (Ivarsson et al., 2020). In miarolitic cavities in pegmatites from the Volyn pegmatite district, Ukraine, genetically associated with the Paleoproterozoic Korosten pluton of the western Ukrainian shield (Fig. 1), fossils occur in a conspicuous filamentous form. They are known as 'kerite' and were first described by Ginzburg et al. (1987) as a result of abiogenic sublimation and polymerization of volatile hydrocarbons from the pegmatite. In Ukrainian-Russian literature this type of organic matter (OM) was characterized as (oxy)kerite, i.e. highly mature OM. Gorlenko et al. (2000) and Zhmur (2003) were the first to re-interpret these kerites as fossils of filamentous cyanobacteria, based on electron microscopic investigations on ultra-thin sections. They also pointed out that cyanobacteria are not the only microorganisms, but they described the occurrence as a microbial community, an 'Early Proterozoic autonomous biocoenosis'. Stable $\delta^{13}C$ isotope ratios $\leq$ -40 ‰ of such filaments are similar to $\delta^{13}C$ isotope ratios in methanogenic bacteria (Franz et al. 2017). Typical for kerite is the high N-content, which goes up to 9 wt% (Luk'yanova et al., 1992; Franz et al., 2017). The maximum age of the fossils is restricted by the 1760±3 Ma intrusion age of the pegmatites (Shumlyanskyy et al., 2021; Fig. 1). The minimum age is constrained by ^{40}Ar-^{39}Ar laser-ablation age data of minerals in a breccia, which formed after consolidation of the pegmatites. This breccia contains degraded OM together with newly formed muscovite (formation age 1491±9 Ma; Franz et al., in review) and buddingtonite, NH_4-feldspar (minimum age of 563±14 Ma). Ammonium ions are a product of the degradation of OM, and the white mica age and the buddingtonite age restrict the age of the organisms most likely near to 1.5 Ga, the age of pseudomorph formation (for detailed discussion see Franz et al., in press). (*Footnote: In the title of Zhmur, 2003, there is an obvious*

73   *typing error: It says "Origin of Cambrian fibrous kerites of the Volyn region", but in the text it*

74   *is clear that the authors refer to a Precambrian age.*)

75   The miarolitic cavities hosting the kerite fossils (Fig. 2) are a special feature of these pegmatites,

76   which are therefore referred to as 'chamber pegmatites' (see reviews in Ivanovich and

77   Alekseevich, 2007; Lyckberg et al., 2009). These chambers are zones of free growth for crystals

78   ('crystal pockets') and were formed in the cooling stage of the pegmatite, in the same way as

79   common miarolitic cavities, i.e. from magmatic fluids, liberated during crystallization. What is

80   unusual is their size: Lyckberg et al. (2019) describe the largest pocket of pegmatite no. 521 in

81   a depth of 96 m with dimensions of 45 m in length, up to 25 m wide and about 20 m high.

82   Common are cavity dimensions of 4 to 6 m in length, 3 to 4 m wide, and 1 to 3 m high (Ivanov

83   and Alekseevich, 2007), and the unusually large size is attributed to the long cooling history in

84   the order of millions of years of the Korosten pluton with supply of fluids from anorthositic

85   magmas (Shumlyanskyy et al., 2021).

86   A striking feature of kerite is the well-preserved morphology (Zhmur, 2003; Franz et al., 2017),

87   which poses the question how the delicate OM without skeletal parts in the organisms was

88   fossilized. Zhmur (2003) interpreted this process as 'hydrocarbon-aqueous fossilization' due to

89   prolonged low-temperature dehydration and oxidation. Here we present data from reflected

90   light microscopy, scanning electron microscopy (SEM), transmission electron microscopy

91   (TEM), and electron probe microanalysis (EMPA) to show that the fossilization process is

92   mainly driven by the reaction of Si-Al-(Ca) with the organisms via a fluid phase rich in F, Cl,

93   S, and P, followed by encrustation of Al-silicates. Attempts to directly date black opal with

94   inclusions of OM and of filamentous kerite using U-Pb-systematics resulted, in the case of opal,

95   in scattered U-Pb data indicative of open system behavior. For the filamentous kerite we

96   obtained a nominally Cambrian minimum age that is consistent with the inferred Precambrian

97   age.

98

99
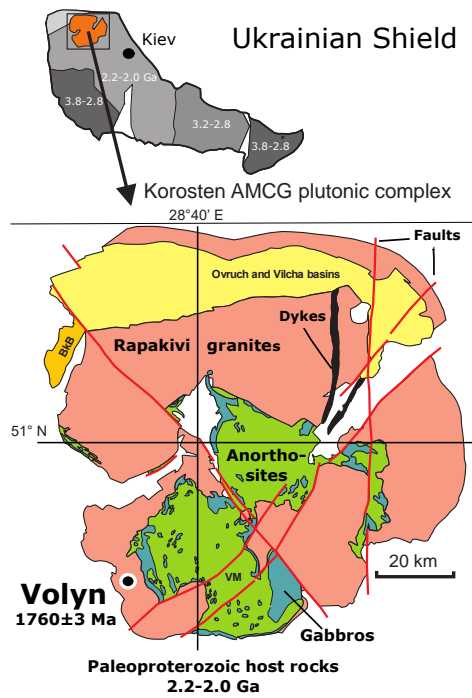
Figure 1: Location of the Volyn pegmatite field in the Korosten anorthosite-mangerite-charnockite-granite plutonic complex, north-western Ukrainian Shield (numbers refer to the ages in Ga of consolidation of the shield; Shumlyanskyy et al., 2017). The pegmatite age of 1760±3 Ma at Volyn refers to zircon U-Pb SIMS data (Shumlyanskyy et al., 2021).

1.1 Sample material and methods

Sample material from the Volyn pegmatite includes kerite, obtained from the Museum of the National Academy of Sciences, Semenenko Institute of Geochemistry, Mineralogy and Ore Formation, Kyiv, and seven kerite samples, sampled underground in situ from the pegmatites (Table 1). Kerite could not be found in the surrounding granite, only in the pegmatite. The microfossils are found free on the surface or partly in the upper layer of clay on the floor of the miarolitic open chamber (Fig.). Kerite occurs there in masses of kg as described in the Russian and Ukrainian literature (Zmuhr 2003, Gorlenko et al. 2000, and references in these papers), as verified by coauthor Chernousenko. It can be found also on the surface of beryl and topaz crystals.

115 In addition, we investigated single crystals of beryl with etch pits, which contain kerite, and use

116 data from a previously investigated sample 2008-V (Franz et al., 2017), a breccia collected from

117 the mine tailings of pegmatite no. 2, which contains degraded OM in a pseudomorph after beryl,

118 consisting of buddingtonite, muscovite, betrandite, and opal. For the age determination, we

119 used this OM together with sample #9 (Table 1; aliquots a,b,c), which is topaz with degraded

120 OM, and black opal (sample BO, subdivided into aliquots) from the same shaft.

121

122 **Figure 2: (a) Kerite-rich in situ occurrence (black; arrows) on wall inside crystal cavity**
123 **chamber in shaft 3 of Volyn Chamber Pegmatite, Volyn Piezo Quartz Deposit,**
124 **Korosten Pluton, Zhitomirskaya Oblast, Ukraine, with chief geologist Vsevolod**
125 **Chournousenko as scale. Photo courtesy of V. Chournousenko.**
126 **(b) Black kerite in situ on wall inside crystal cavity chamber. Photo by Vsevolod**
127 **Chournousenko.**

128

129 SEM images were obtained with a Hitachi SU8030 instrument, equipped with an EDAX EDS

130 system with a 30 mm^2 silicon drift detector (SDD) fitted with a silicon nitride window. We first

tried to work without coating but the filaments are non-conductive and were electrically

charged. Samples were therefore coated with an approximately 5 nm thick Ir layer allowing for

high-resolution imaging of the filaments' surfaces without a structure of the commonly applied

Au coating. The kerite filaments without further cleaning or preparation were mounted on Al

stubs stickered with conductive carbon tabs. The beryl crystals with kerite filaments were dust-

cleaned with compressed air and coated with C.

Table 1: List of samples and their macroscopic appearance

No./GFZ no.	Year of sampling	Material	Location	Morphology
0/Museum Ac. Sci. Kyiv	unknown	kerite	unknown	filamentous
1/G017809	2018	kerite	shaft 3	filamentous
2/G017810	2018	kerite	shaft 3	filamentous
3/G017811	2018	kerite	shaft 3	filamentous
4/G017812	2018	kerite	shaft 3	filamentous, spherical
5/G017813	2013	kerite	shaft 3	flaky, botryoidal
6/G017814	2013	kerite	shaft 3	filamentous, flaky
7/G017815	2013	kerite	shaft 3	filamentous, spherical
2008-V-10	2008	beryl crystal with etch pits	mine tailings pegmatite #2	filamentous, spherical, flaky
9a,b,c	2018	topaz with kerite	shaft 3	(degraded kerite)
BO	2018	black opal	shaft 3	(inclusions of OM)
2008-V-1,a,b,c	2008	pseudomorph after beryl	mine tailings pegmatite #2	(degraded kerite)

The JEOL JXA-8530F field emission microprobe at TU Berlin was used to investigate the same

mounts that were used for reflected light microscopy, but with C-coating, for quantitative

results and less absorbance (compared to Ir). EPMA data for element distribution maps of cross

sections or of parts of the rim of the filaments and flaky kerite in the wave-length dispersive

mode of the microprobe were acquired using an 8 kV, 20 nA beam with a probe diameter of 64

nm. Back-scattered electron images (BSE) were taken to select appropriate sites. Mappings

were done in stage scan-modus with pixel resolution between 277 and 360 x 180 and 265, with

147 a pixel size of mostly 80 nm, and a dwell time per pixel of 200 ms. Total scan areas varied

148 between 70 x 36 µm to 33.2 x 31.8 µm.

149 Open-system pyrolysis was performed using a Quantum MSSV-2 Thermal Analyzer©

150 interfaced with an Agilent GC 6890A gas chromatograph. Milligram quantities (0.3-2.0 mg) of

151 freshly powdered sample material were weighed into the central part of small glass capillaries

152 and fixed with purified quartz wool that had been cleaned by heating at 630°C in air for 30 min.

153 Open-system pyrolysis was performed from 300°C to 600°C at 40°C/min in a flow of He at a

154 rate of 30 mL/min. The generated hydrocarbons were immediately transferred to a liquid

155 nitrogen cooled trap and subsequently analyzed using an Agilent GC 6890A gas chromatograph

156 equipped with an HP-Ultra 1 column of 50 m length, 50m x 32mm internal diameter,

157 dimethylpolysiloxane-coated column (0.52 µm film thickness), and flame ionization detector.

158 The oven temperature was programmed from 30°C to 320°C at 5°C/min. Qualification of single

159 compounds was conducted using reference chromatograms.

160 For the U-Th-Pb analysis, fragments of OM from two samples were selected under a binocular

161 microscope. Fragments from sample No. 9 were visually pure, inclusion-free, with a dark

162 brownish color. Fragments from sample No. 1 showed fine-grained intergrowth with colorless

163 to whitish phases, probably quartz and feldspar. After cleaning in double-distilled water in an

164 ultrasonic bath, fragments (weight between 0.38 and 2.53 mg) were digested in 68%-HNO_3 at

165 220°C for 48 h using a Parr-type hydrothermal digestion vessel, a procedure that has been

166 shown to effectively mineralize a broad range of organic matter (Tahán et al., 1993). Optical

167 control revealed that all OM was fully dissolved in this step. Sample solutions were dried and

168 re-dissolved in 2%-HNO_3. Concentrations of U and Th were measured by isotope dilution on a

169 Thermo Scientific ELEMENT XR ICP-MS at GFZ Potsdam, using a mixed ^{235}U-^{230}Th spike.

170 Concentrations of lead isotopes ^{204}Pb, ^{206}Pb, ^{207}Pb, and ^{208}Pb were determined on the same

171 instrument from sample signal count rates compared to an external calibration curve for Pb.

172   Corrections for background and for interference of ^{204}Hg on the ^{204}Pb signal were applied.

173   For TEM investigations foils were prepared using focused ion beam (FIB); for details of milling

174   see Wirth (2004, 2009). They were studied in a Tecnai F20 X-Twin TEM operated at 200 kV

175   with a field emission gun as electron source, equipped with a Gatan imaging filter GIF™

176   (Tridiem), a Fishione high-angle annular dark field detector (HAADF), and an EDAX X-ray

177   analyzer with ultra-thin window. Bright field, dark field and high-resolution TEM images are

178   usually acquired as energy-filtered images applying a 20 eV window to the zero loss peak of

179   the electron energy-loss spectrum. Counting time for EDS analyses (processed with TIA™

180   software) in the scanning transmission mode across a pre-selected area thus avoiding mass loss

181   during the data acquisition, was 60 to 120 s. Electron diffraction data were acquired as selected

182   area electron diffraction pattern (SAED) or derived from high-resolution lattice fringe images

183   applying a fast Fourier Transform (FFT). Electron energy loss spectra (EELS; data processing

184   with Digital Micrograph™) were acquired in diffraction mode using a camera length of 700

185   mm. Applying a 1 mm entrance aperture the resulting acceptance semi angle is 5 mrad.

186   Dispersion was 0.1 ev/pixel, acquisition time was 1 s.

187

188   **2 Results**

189   **2.1 SEM images**

190   The kerite morphology is best illustrated in SEM images (Fig. 3). There are three different types

191   of morphologies, classified as filamentous, often branched (Fig. 3a,c), as spherical (Fig. 3b),

192   and irregular, flaky objects (Fig. 3c). Objects with spherical morphology are rare, therefore we

193   restrict to the filaments and flakes, which could also be found in thick sections of kerite

194   embedded in epoxy, and thus available for more detailed analytical investigations. Filaments

195   are the dominant forms. Broken pieces are up to ~1 cm long and have a variable diameter, from

196   1-2 μm up to c. 80 μm, mostly near c. 15-20 μm. Many of the filaments are branched (Fig. 3d),

197 or segmented (Fig. 3e,f) and show globular outgrowths, some of these outgrowths with

198 botryoidal shape (Fig. 3e). This botryoidal shape can extend into more irregular, ridged forms.

199 Flaky kerite is best seen in etch pits of beryl from Volyn (Fig. 3a,c), attached together with

200 filamentous and rare spherical objects to the surface of beryl.

201 In many cases we see minerals grown onto the filaments, identified by chemical composition

202 and shape as e.g. kaolinite and chlorite (Fig. 4a), illite and Na-Al-silicate (Fig. 4b); for

203 documentation of the EDS spectra see Supplementary Information Fig. SI 1. On filaments with

204 a rather smooth surface we see structures in the order of 100 x 500 nm which are enriched in

205 Al, Si, Fe, and S, probably pyrite/markasite with Si-Al-incrustations (Fig. 4c). Segmented

206 filaments (Fig. 4d) show larger structures and the EDS analysis indicates incrustations of clay

207 minerals such as illite/kaolinite. In many spectra, the peak of Ir is relatively broad and this might

208 be an indication for overlapping with a P-peak. As we show later (results of EMPA), P is indeed

209 present in the kerite rims. The matrix between filaments consists of opal, intergrown with

210 silicates, probably Na-feldspar, and clay minerals (Fig. 4e,f). In several cases, fluorite crystals

211 could be identified together with the incrustations. In this case, there are also traces of Ca in the

212 incrustation.

213
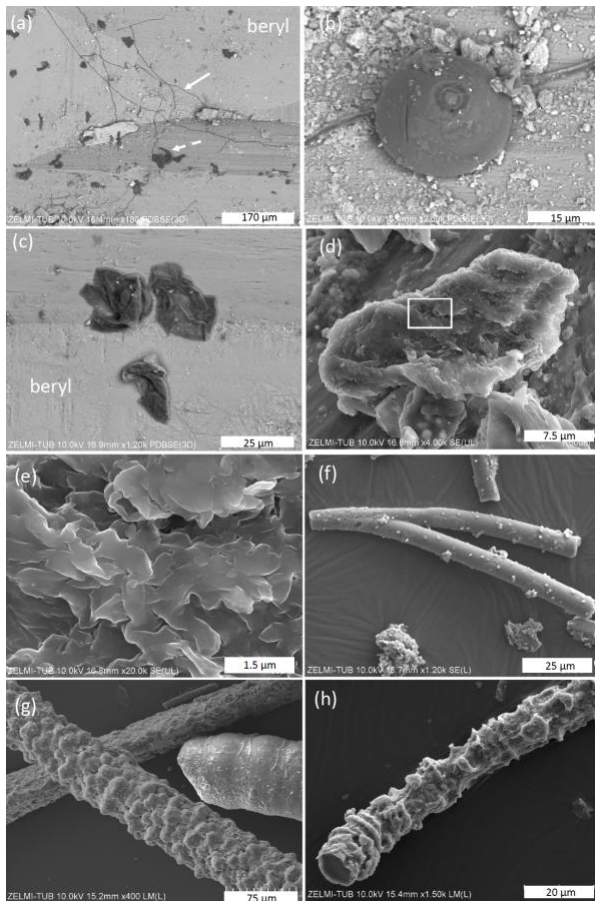
Figure 3: SEM images of kerite fossils, illustrating the different morphologies. (a) Filamentous and flaky kerite in etch pits of beryl (sample #10). (b) Spherical object on a filament (sample #10). (c) Flaky kerite (sample #10). (d, e) enlarged particle of flaky kerite; white rectangle indicates position of (e). (f) Branched filament with smooth surface (sample #4). (g) Filaments with a botryoidal and a smooth, slightly segmented surface (sample #5). (h) Fiber with a strongly segmented surface (sample #2). EDS-spectra of flaky kerite are shown in Fig. SI 2.

222
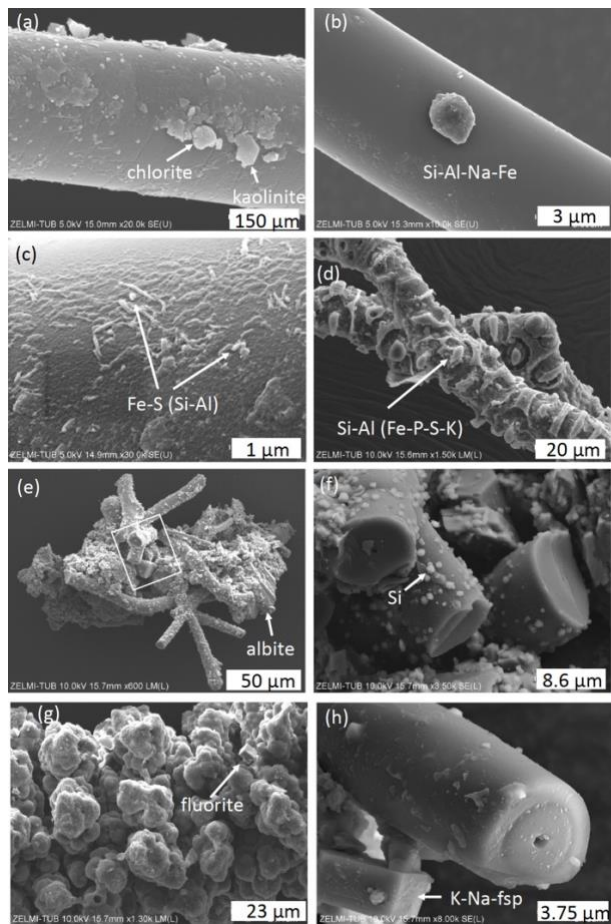
Figure 4: SEM images of minerals, associated with kerite. (a) Chlorite and kaolinite, and (b) unidentified Na-Fe-Al-silicate grain grown onto a filament (sample #0). (c) High-magnification of filament surface with Fe-sulfide (pyrite/markasite?) and incrustations of Si-Al (sample #0). (d) Incrustation on segmented filament, with dominantly Si-Al, minor peaks of Fe-P-S-K (sample #4). (e) Aggregate of filaments, cemented by minerals; lower right is an albite crystal; rectangle shows position of (f), enlarged part with broken filaments and small opal grains (identified by a Si-peak and globular shape) attached to the surface (sample #4). (g) Aggregates forming a botryoidal surface of a filament, intergrown with a fluorite crystal. (h) Alkalifeldspar, grown onto a broken filament with central cavity.

The surface of botryoidal shapes (Fig. 5a) shows µm-wide gaps, explained as shrinking cracks, and ball-shaped outgrowths (Fig. 5b,c) with a dented surface, interpreted as a result of degassing of the OM. The EDS-spectra of this surface shows peaks for Al and Si, in addition to the C-N-O-content of kerite. The internal structure of kerite is seen in a broken face of a filament; it is characterized by a porosity (Fig. 5e-h), also interpreted as result of degassing. Individual pores are irregular in shape and in the order of several 100 nm large (Fig. 5g,h). In cross section, some of the broken filaments show a central cavity, i.e. a channel extending along the filament axis

241 (Figs. 4h, 6). The cross sections of this channel vary from c. 250 x 500 nm (Fig. 6a) to c. 20 x

242 20 µm (Fig. 6f) in diameter. In some cases, the channel has a six-sided outline (Fig. 6f,g,h).

243 The fractured surface with fringe fractures, sub-perpendicular to the filament length (Fig. 6a,g),

244 indicates brittle behavior of the filaments, which was also observed during handling the

245 individual filaments for preparation. Figure 6d shows a broken filament with a sheath-like outer

246 part. The outer rim (with a dented surface, seen in its lower part) contains some Al-Si, a small

247 amount of K and possibly P (Fig. SI 4 analyses 2 & 5); the inner rim shows only traces of Al-

248 Si, but some U (analyses 3 & 4), whereas the center near to the channel (analysis 6) shows only

249 the peaks of C-N-O, characteristic for kerite. The count ratios for C/O increase systematically

250 from outer rim to the center (Fig. SI 4).
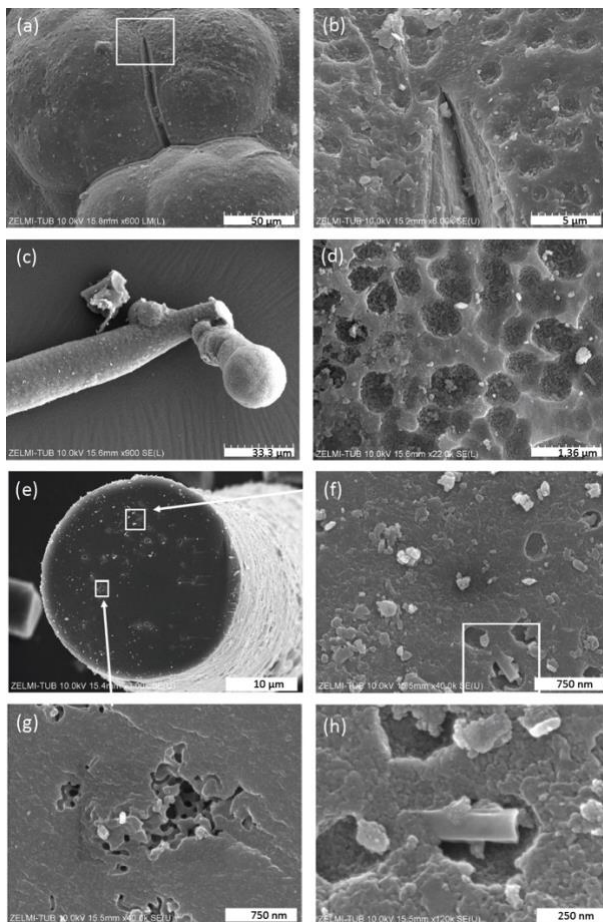
251

252 **Figure 5: SEM images of surfaces of kerite. (a) Botryoidal surface with a shrinking crack;**
253 **inset shows enlarged part in (b) with a dented surface (sample #5). (c) Ball-shaped end of**
254 **a filament, with (d) dented surface (sample# 1). (e) Broken filament (sample #3), showing**
255 **internal porosity (f,g,h) with irregular outlines, of a few hundreds of nm wide. White**
256 **rectangle in (f) indicates enlarged part shown in (h).**
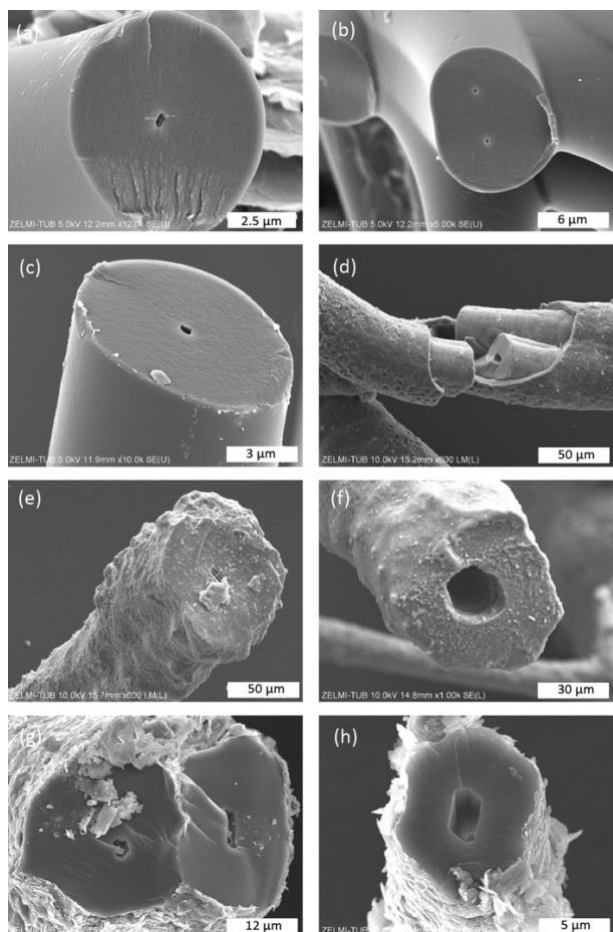
257

258 **Figure 6: SEM images of broken filaments, showing a central channel. (a) Six-sided**
259 **channel with dimensions 260 x 550 nm of filament with a smooth surface, and fringe**
260 **fractures on the broken face, indicating brittle behavior. (b) Double channel, probably**
261 **initial crosscutting of a branching (cf. Fig. 4d). (c) Similar channel as in (a), but less**
262 **regular outline (all sample #0). (d) Filament with a central part, a sheath-like outer part,**
263 **and a channel; numbers refer to analysis points (see text; EDS spectra in Fig. SI 4). Note**
264 **dented surface in lower part of the sheath-like outer part (sample #5). (e) Filament with a**
265 **rough surface and a channel 4 x 11 μm. (f) Large, ca. 25 μm wide channel with six-sided**
266 **outline (both sample #5). (g,h) Filaments with encrustations of clay minerals and six-sided**
267 **channels (sample #7).**

268

269 **2.2 Reflected light microscopy**

270 In two-dimensional cuts in polished mounts in epoxy, observed under UV light for fluorescence

271 and under white light for reflectivity (Fig. 7), the clear outer circular (to elliptical in oblique

272 sections) shape of filaments is obvious in cross sections (Fig. 7a). In longitudinal sections (Fig.

273 7b), the symmetrical internal structure, which shows up in the cross sections, extends along the

274 whole filament. There are mainly three zones, an outer discontinuous, thin rim with a higher

275 reflection/lower luminescence (zone 1), followed by a zone 2 with poorer reflection, higher

276 fluorescence, and a core zone 3 with low fluorescence/intermediate reflectivity. The central,

277 open channel with different width is also seen in many filaments (Fig. 7a). Ball-shaped

278 outgrowths show the same type of zoning as the filaments. Flaky kerite is seen as a thin (a few

279 µm wide) (bio?)film, intergrown with mineral matrix (Fig. 7c). Botryoidal shapes show

280 difference in reflectivity which runs parallel to the surface (Fig. 7d) and with highest reflectivity

281 around pores. Thick, irregularly shaped masses, possibly degraded OM (Fig. 7e,f) show rims

282 high in reflectance and zonal distribution of luminescence in UV light.
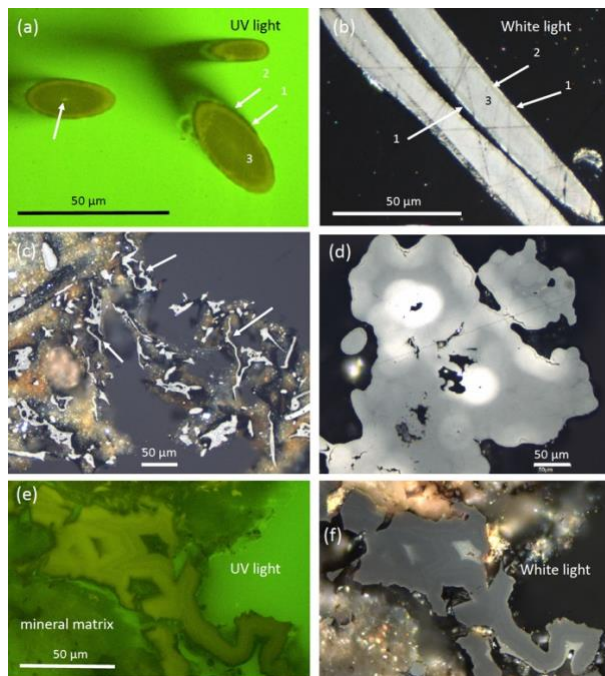
283

284 **Figure 7: Optical reflected light microscopy of polished grain mounts, under UV light for**
285 **fluorescence and under white light for reflectance. (a) Cross section of filaments, with a**
286 **central channel (left arrow) and three zones of fluorescence. (b) Longitudinal sections**
287 **show a symmetrical distribution of the three zones in reflectance, where the rim with high**
288 **reflectance corresponds to the rim with low fluorescence shown in (a). (c) Thin flaky**
289 **kerite, interpreted as former biofilms (arrows). (d) Botryoidal kerite with zonal**
290 **distribution of reflectivity. (e, f) Thick masses of flaky kerite with zonal fluorescence and**
291 **reflectivity.**

292

293 **2.3 Electron microprobe analyses (EMPA)**

294 The same mounts prepared for reflected light microscopy were used for EMPA. Within the

295 mineral matrix, we confirmed the presence of fluorite, closely intergrown with kerite, and also

296 identified buddingtonite, characterized by zoning and a significant decrease of the NH_4-
297 component from core to rim (Fig. SI 4).

298 In order to show the distribution of elements in kerite by element mapping with EMPA, we
299 chose two cross sections of filaments (Fig. 8); the outer part of a large, segmented filament (Fig.
300 9); a botryoidal part with ball-shaped outgrowths on more irregularly shaped kerite; and the rim
301 of flaky kerite (Fig. 9). BSE images for location of the mapping areas in the selected grains are
302 shown in the Fig. SI 5. Mapping included the characteristic elements identified before with
303 SEM-EDS, i.e. O-N as part of kerite (C was not mapped because samples were C-coated), S
304 and P, which can be part of kerite, but were also observed on the surface as sulfate or phosphate
305 minerals (see above, SEM investigations), and Si, Al, and Ca as characteristic for silicates. Cl
306 was mapped, because we found it also on the surface of the OM in the etch pits in EDS analysis,
307 but was below detection level in the element distribution maps. Because the OM is very
308 sensitive to the electron beam (see image after mapping in Fig. SI 5c), we chose a trade-off
309 between high resolution, X-ray excitation, and measuring time, but nevertheless, beam-related
310 damage could not be completely avoided.

311 An oblique section of a 15 µm-wide filament (Fig. 8) shows O enriched in the upper right part,
312 where N and S are low, indicating simultaneous N and S loss during progressive maturation.
313 During maturation of OM labile nitrogen and sulfur-bearing compounds are converted and lost
314 whereas oxygen-bearing macromolecules are enriched (Poetz et al., 2014). Here, mineralization
315 of the organic fraction was preservative due to aromatization and this process caused formation
316 of oxygen-bearing aromatic macromolecules. However, S is low in the area in the lower left
317 with lowest BSE-contrast and where N is concentrated. Si and Al concentrated in the outer,
318 irregular and discontinuous rim, together with O, present as Al-silicates as determined by SEM.
319 The Ca-distribution is complex; it is enriched in the rim, but does not follow Si-Al. Instead, it
320 forms an inner rim. It is also concentrated in the lower left part of this filament, in the same

321 area, where S is enriched. P shows some enrichments in spots in the inner part and in the rim,

322 together with Ca interpreted as Ca-phosphate. Similar element distributions were observed in a

323 circular section of a filament (Fig. SI 6).
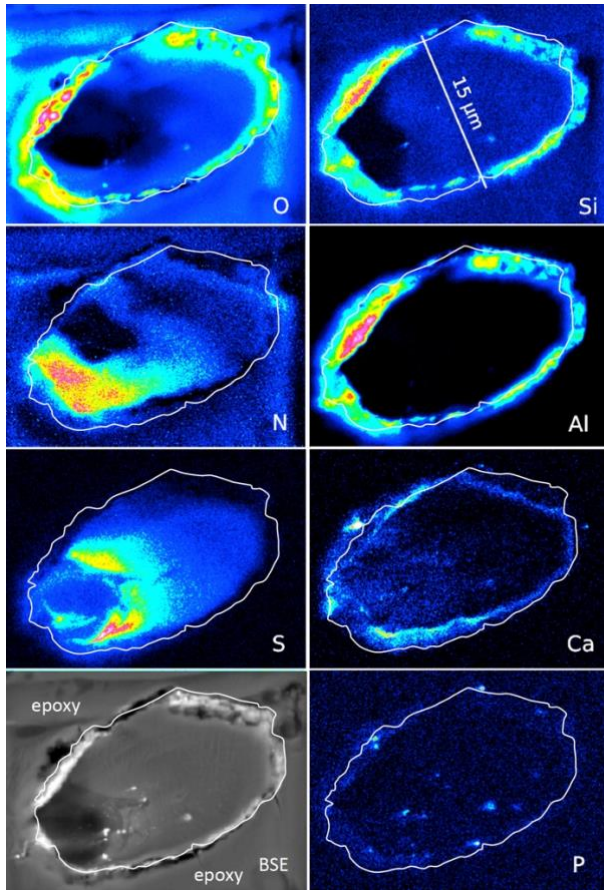
324

325 **Figure 8: Element distribution (EMPA) of an oblique section of a 15 μm-wide filament,**
326 **embedded in epoxy. White line indicates outermost rim of the filament, as seen in the BSE**
327 **image. BSE-contrast is lowest in the area of low O, high N content. Si and Al (with O)**
328 **form an outer rim, indicating Al-silicates (probably clay minerals, as determined by**
329 **SEM). Ca is also concentrated in the rim, but also in spots together with P and in the area**
330 **with high S. Scanning conditions: pixel resolution of 360 x 265, pixel size of 80 nm, dwell**
331 **time per pixel of 200 ms, total scan area 28.8 x 21.2 μm.**

332

333 The outer rim of a segmented filament (Fig. 9) allows a sharper differentiation compared to the

334 observations above: Si, Al, O are concentrated in the outer, irregular and discontinuous rim,

335 together with Ca, which is enriched in spots together with P, but also with S (probably forming

336 Ca-sulfate); S is enriched together with Ca in the outer rim. The outer rim is followed by an

337 inner rim 1, poor in Ca, and then by an inner rim 2 with Ca-enrichment. O distribution is highest

338 in the outer rim, high in the inner rim 1 with a rather sharp boundary to the inner rim 2, and

339 then diffuse into the central part. N shows a relatively homogeneous distribution, but occurs up

340 to the outer rim in areas of Si-Al concentrations, indicating the formation of NH_4-minerals

341 (buddingtonite, tobelite).
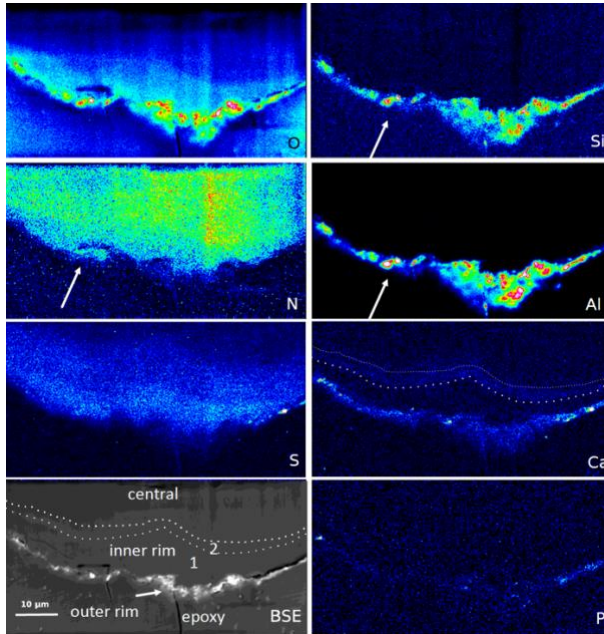
342

343 **Figure 9: Element distribution (EMPA) of the rim of a large filament. The rim consists of**
344 **three areas, best visible in the BSE and Ca image: an outer, irregular and discontinuous**
345 **rim with enrichment of Si-Al-O and Ca, an inner rim 1, poor in Ca, followed by an**
346 **approximately 1-2 μm wide inner rim 2, enriched in Ca (dotted lines). In the outer rim,**
347 **Ca is also concentrated together with P and S. N distribution is relatively homogeneous,**
348 **but notably extends up to the outer rim, together with Al-Si (arrows), indicating**
349 **formation of NH_4-minerals (buddingtonite, tobelite). Vertical stripes are due to beam**
350 **damage. Scanning conditions: pixel resolution 350 x 180 with pixel size of 200 nm and a**
351 **dwell time per pixel of 200 ms, total scan area 70 x 36 μm.**

352
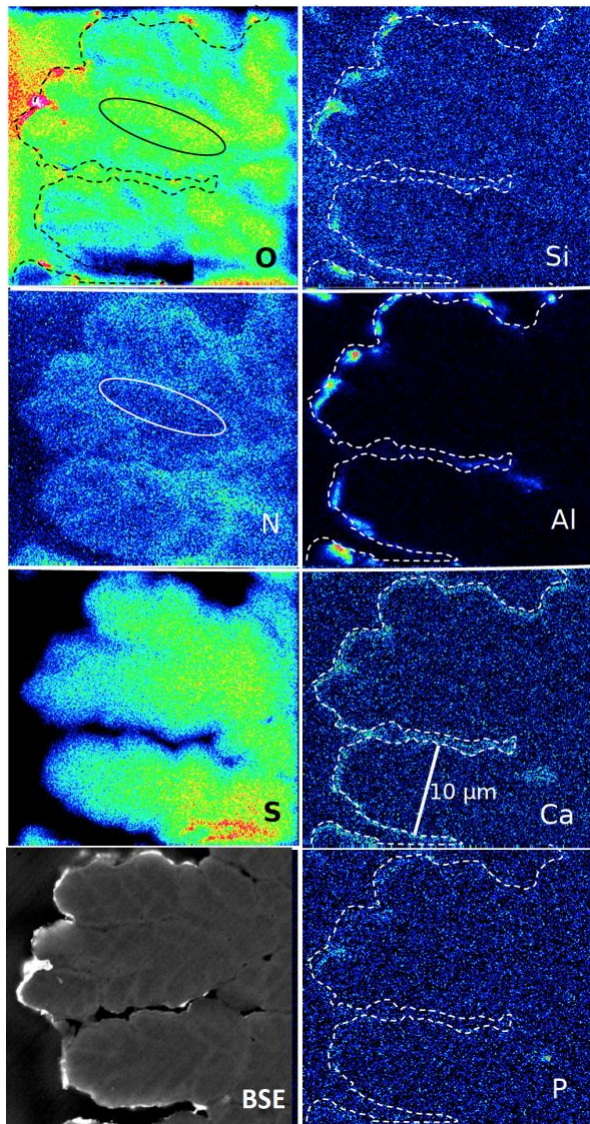
353

354 **Figure 10: Element distribution (EMPA) in botryoidal kerite. The rim (dashed line) is**
355 **outlined as seen in the BSE image. Si, Al, and O are concentrated in a discontinuous rim,**
356 **indicating Al-silicates. Ca is concentrated in spots in this rim together with P, indicating**
357 **Ca-phosphate. Sulfur decreases systematically from the central part to the rim. N**
358 **distribution is heterogeneous, and mimics the BSE contrast. Areas rich in O are poor in**
359 **N (see oval outlined area). Scanning conditions: pixel resolution of 277 x 265 with pixel**
360 **size of 120 nm and a dwell time per pixel of 200 ms, total scan area 33.2 x 31.8 μm.**

361

362
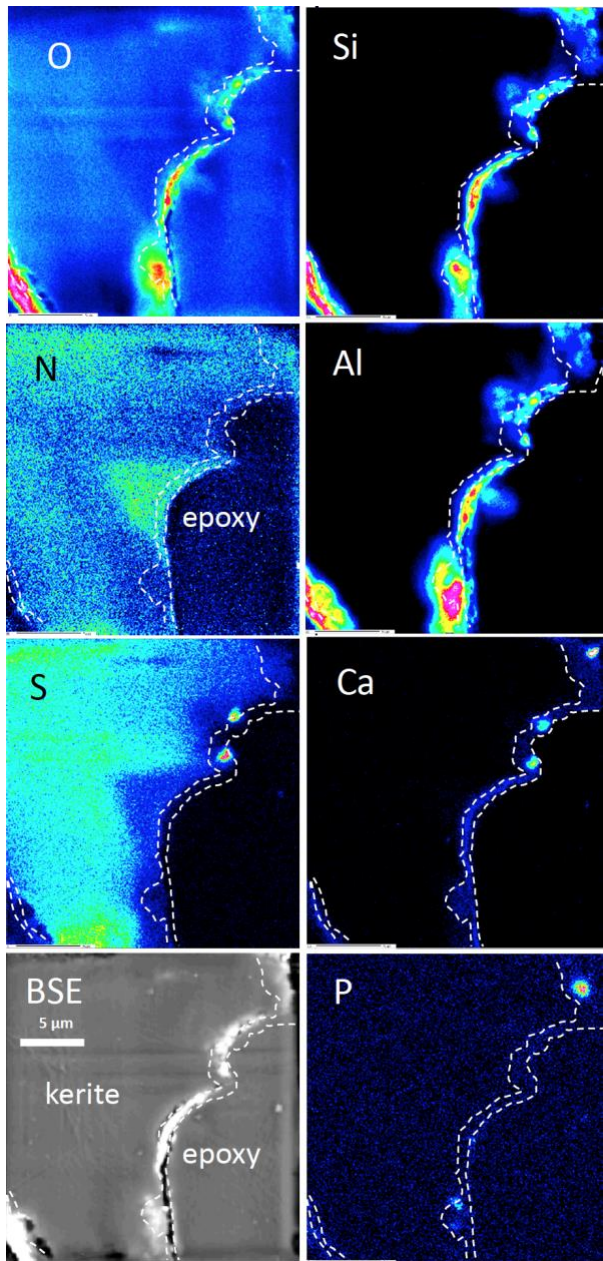
Figure 11: Element distribution (EMPA) of the rim of flaky kerite. The rim is outlined as seen in the Ca image. Si, Al, and O are concentrated in a discontinuous rim, indicating Al-silicates. Ca is concentrated in spots together with P and S, indicating Ca-sulfates and Ca-phosphates, but also in a continuous rim with concentrations slightly above the background. Sulfur - except for the enrichment in spots - is absent in this area, and also less concentrated near to the rim. N distribution is heterogeneous, but as in Fig. 9 can extends up to the outer rim. Areas rich in N are poor in O.

The element distribution in botryoidal kerite (Fig. 10) is characterized by an internal, heterogeneous N distribution, anticorrelated with O, which is visible in the BSE contrast. Sulfur systematically decreases from the central part towards the rim. Calcium is enriched in a thin rim, associated with P in a few spots as Ca-phosphate. The element distribution in flaky kerite

375 (Fig. 11) is generally similar to the observations made in filaments. Al-silicates form an outer,

376 discontinuous rim, Ca is slightly above the background in the rim, but also forms discrete, small

377 ($\leq$ 1 µm) Ca-sulfates and Ca-phosphates. Sulfur is absent (except for the enrichment in Ca-

378 sulfates) in this rim, indicating loss of S during maturation/fossilization. Towards the interior

379 of the flaky OM, distribution of N, O, and S is heterogeneous, a possible indication for a primary

380 (biological) character, combined with loss of N during degradation. A different flaky object

381 shows similar element distributions (Fig. SI 8), however the phosphatization in the outermost

382 rim is more pronounced than in the other element distribution maps.

383 **2.4 TEM investigations**

384 TEM investigations of FIB-cut foils from a filament, with the foil cut parallel to the elongation

385 of the filament. In the center (Fig. 12) it shows the amorphous character and the presence of Si

386 together with C-N-O-S. In the rim, infiltration of Si, Al, and Ca, but in addition also Mg, Fe,

387 K, and Ni in the whole filament could be confirmed (Fig. SI 8); N was also confirmed by EELS

388 analysis (Figure SI 8) in the dominantly C-rich matrix.
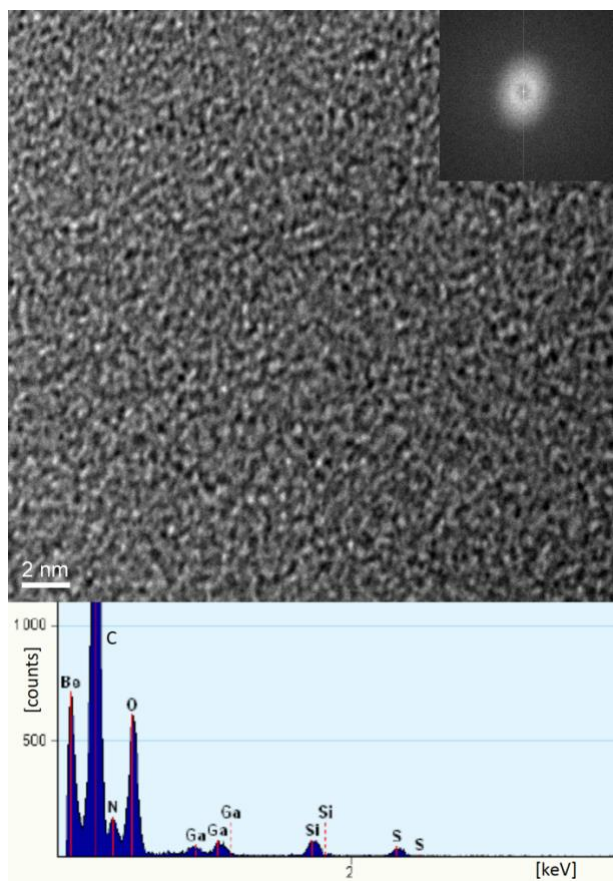
389

390 **Figure 11: HRTEM-image of central part of a filament, showing amorphous kerite (inset**
391 **is electron diffraction pattern) and EDS-spectrum of a spot, confirming Si as an impurity,**
392 **C-N-O and S as the kerite constituents. Ga-peak is from cutting of the FIB foil, Be is from**
393 **the Be-sample holder.**

394

395 **2.5 Pyrolysis**

396 Results of open-system pyrolysis are consistent with other observations, indicating mature or

397 very mature OM, and there is no essential difference between samples with well-preserved

398 shape and others with many incrustations. The gas chromatographic fingerprints of sample #0

399 are shown in Fig. 13, the results of the other samples are in Fig. SI 9.

400 All are strongly dominated by hydrocarbon gases C_{1-5} (methane through pentane) and

401 subordinately by alkylated mono- and diaromatic compounds. These are typical pyrolysis

402 breakdown products of organic matter in general, but as higher n-alkyl homologues (n-C_{6+}) or

403 oxygen-, sulphur-, and nitrogen-functionalized compounds (e.g., phenols, thiophenes, and

404 carbazoles) as indicators of biological precursor structures (Larter, 1984; Horsfield, 1989;

405 Sinninghe Damsté et al., 1989) are essentially absent they are indicative of mature OM. Loss

406 of functional groups during diagenesis and loss of H-rich components during catagenesis leads

407 all organic matter types to move towards the point (metagenesis) where they become

408 indistinguishable finally possessing only a potential for the generation of dry gas (methane) and

409 mono aromatic compounds (Tissot and Welte, 1984; Quigley and Mackenzie, 1988; England

410 and Mackenzie, 1989; Horsfield, 1989). In line with remaining fluorescence the composition

411 of the pyrolysate, especially presence of wet gases (C_{2-5}) and diaromatic compounds, indicates

412 that the OM has not yet arrived at metagenesis ($R_o > 2.0\%$, where R_o = vitrinite reflectance in

413 oil (Tissot and Welte, 1978). GC-fingerprints resemble e.g. those of Paleozoic coals and shales

414 from Australia at $1.7\% < R_o < 2.3\%$ (Mahlstedt et al., 2014, 2015). Assuming typical geological

415 heating rates between 1 and 3K/Myr and based on the easyR_o model (Burnham and Sweeney,

416 1989). OM at these maturity levels must have been heated to somewhere between 175 and

417 200°C; a similar temperature range was also derived from mineral equilibria (Franz et al.,

418 2017). In case that peak temperatures were very short-lived, temperatures could have been

419 slightly higher, but the time duration for the maturation of the Precambrian fossils is essentially

420 unknown.
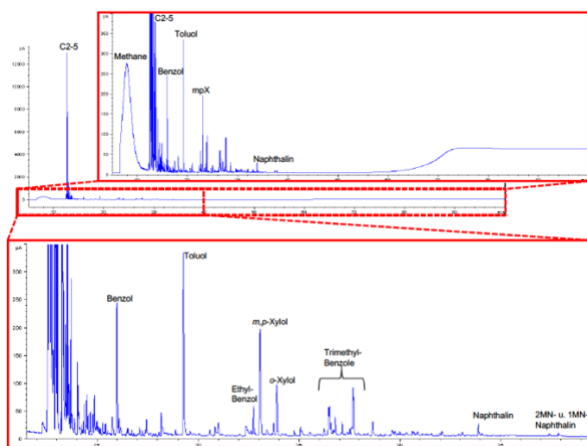
421

422 **Figure 12: Open-system pyrolysis GC-trace of kerite (sample #0/Museum Ac. Sci. Kiev),**
423 **is dominated by hydrocarbon gases methane through pentane and subordinately by**
424 **alkylated mono- and diaromatic compounds, typical breakdown products of mature or**
425 **very mature OM.**

426

 2.6 U-Th-Pb analyses

428 Table 2: Results of Pb isotope data of aliquots of OM, sample 9 (visually pure oxykerite) and

429 sample 1 (impure with whitish minerals)

sample	weight (g)	$^{206}Pb/^{204}Pb$	RSD%	$^{206}Pb/^{207}Pb$	RSD %	$^{208}Pb/^{204}Pb$	RSD%
UKR 1 9-a	0.00253	477.3	5.3	42.83	10.63	5.32	108.5
UKR 2 9-b	0.00090	36.46	3.5	17.04	2.132	2.01	42.46
UKR 3 9-c	0.00101	320.2	10.2	33.39	8.925	4.78	85.19
UKR 4 1-a	0.00038	51.00	0.9	18.45	2.753	1.61	70.18
UKR 5 1-b	0.00043	53.22	1.5	18.61	2.870	1.07	73.17
UKR 6 1-c	0.00067	47.43	0.9	18.01	2.634	1.41	64.14

430
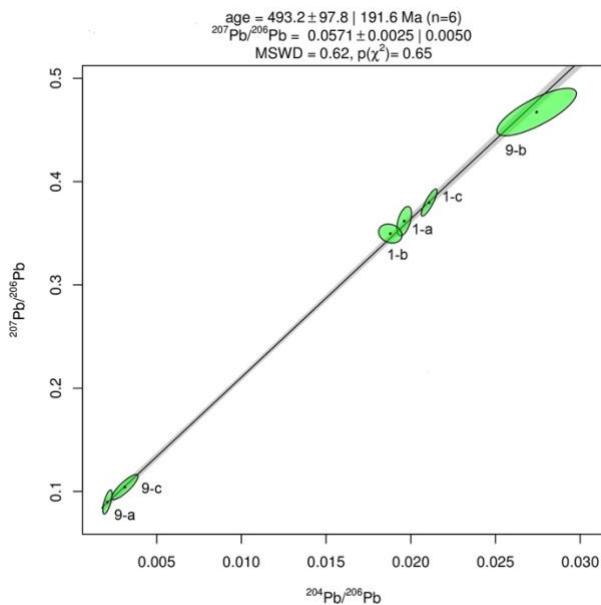
431

432 **Figure 14: Results of Pb-Pb age determination of kerite from Volyn pegmatite. The**
433 **reference line corresponds to an age of 493.2 ± 97.8 Ma (1σ). The large uncertainty is**
434 **mainly due to very small amounts of Pb in the samples, resulting in poor ion counting**
435 **statistics in mass spectrometry. Data plotted and age calculated using the program**
436 **Isoplot-R (Vermeesch, 2018).**

437

438 Results of Pb isotope analyses of kerite samples 9 and 1 and the OM from the pseudomorph

439 sample are listed in Table 2 and shown in Fig. 14. The reference line corresponds to an age of

440 493.2 Ma, however with a large uncertainty of ± 97.8 Ma (1σ). The apparent age is considered

441 as a minimum age, because OM is very susceptible for U, which is likely present in the fluids

442 circulating in the pegmatitic environment since formation of the miarolitic chambers until

443   modern times, a process that is capable to continuously reset U-Pb dates.

444   Chemical and U, Th, and Pb isotope data of black opal are presented in Tables SI 1 to SI 3.

445   Major element analyses (Table SI 1) in opal indicate approximately 2.5 wt% undetermined

446   elements, likely H_2O and hydrocarbons. Minor elements are Al (up to 1 wt% Al_2O_3), Na, Ca,

447   and Fe, which are present in 0.1 to 0.3 wt% oxide, whereas Ti, K, Mg, Fe, Cr, V, and Mn occur

448   in smaller amounts. The heterogeneous distribution of elements is also seen in the trace element

449   content among the three aliquots; Ba, Be, Li, Rb, Sc, Sr, Th, U, V, Zn, and Zr stand out with

450   content each above 1 µg/g in some of the aliquots. The U-Th-Pb isotope data (Table SI 3)

451   indicate open system behavior also for the black opal. The data show a large scatter; only two

452   sample pairs allowed calculating old $^{208}Pb/^{232}Th$ ages of 1500±46 Ma and 1279±35 Ma,

453   respectively.

454   **3 Discussion**

455   **3.1 Fossilization process**

456   A further determination of the exact nature of the excellently preserved microbial fossils

457   requires a distinction between primary, i.e. biological, features and secondary, i.e. those

458   produced by fossilization. The nature of the fossils (bacteria, archaea, or fungi), which

459   colonized the igneous rocks, is not yet clarified; it requires more research, also with more details

460   on spherical kerite, which is in progress.

461   Kerite is highly mature, as shown by pyrolysis experiments (Fig. 13), but not transformed into

462   graphite, as shown by TEM investigations. It is completely amorphous (see in HRTEM image;

463   Fig. 12), indicating rather low temperatures during fossilization and afterwards. This is also

464   consistent with the observation that thin filaments are not completely opaque, but dark-brown

465   transparent, confirming Luk'yanova et al.'s (1992) observations. Their X-ray data of kerite

466   showed a diffuse maximum at c. 8 °θ, interpreted as a mixture of different carbohydrates with

467   O, N, and S, some graphite-like sheets, hexamethylene and polymerized carbohydrates with O.

468   The fringe fractures (Fig. 6a) show that the filament behaved brittle, i.e. the whole filament has

469   reached a similarly high degree of aromatization, which relates to high thermal maturity.

470   Alteration by progressive maturation (e.g., the oxygen pattern along interfaces or affecting the

471   whole kerite matrix) as a major feature is also seen in the element distribution (Figs. 8-11).

472   Sulfur can form Ca-sulfates, as seen in µm-sized spots in the rim, but is generally decreased

473   towards the rim; more detailed mapping of the element distribution in the outer rim area shows

474   Ca enrichment in spots parallel with S, but also with P (Fig. 9, Fig. SI 7), and we speculate

475   about the presence of both, Ca-sulfate and Ca-phosphate nano-scale inclusions due to

476   infiltration of Ca and reaction with of S and P. Sulfur and P were transported out of the filament

477   and reaction with Ca produced the Ca-free inner rim 1. Transport of Ca went further into the

478   filament producing the inner rim 2. Phosphatization, a common fossilization process (e.g.

479   Briggs, 2003) is thus only a minor feature. Alternatively, the Ca distribution in the outer part of

480   the filament might mimic a primary feature, preserved from their growth.

481   The distribution of Si-Al (together with O) is most conspicuous and restricted to a rim of ~ 1 -

482   2 µm width (Figs. 8-11). The presence of Si-Al is confirmed by analytical data with SEM (Fig.

483   6d) and TEM (Fig. 12), and suggests that silicification is the first-order process of fossilization.

484   The patchy distribution indicates the formation of Al-silicate minerals, probably kaolinite or

485   related phases. These patches were observed on the surface of the filaments as vermicular

486   structures (Fig. 4c), some with clear development of crystal faces (Fig. 4a) and continue into

487   more coarse-grained features, which we call encrustations (Fig. 4d). Finally, the patches change

488   into intergrowths of minerals, which could be characterized by shape and chemistry as alkali-

489   feldspar, clay minerals, opal, Fe-sulfides, and fluorite (Fig. 4e-h).

490   We interpret the porosity observed on the surface of botryoidal structures and ball-shaped

491   outgrowths on filaments (Fig. 5c,d) and on a broken cross section (Fig. 5e-h) as degassing

492   features. The irregular internal pores on the scale of a few hundred nanometers indicate irregular

pathways of the gas, transitional towards the outer part into more regular, circular and larger pores of 1 to 2 µm in diameter. We interpret cracks in the surface (Fig. 5a,b) as a shrinking phenomenon, and the irregular shape of flaky kerite on the etch pits of beryl (Fig. 3a,c) as a shrinking phenomenon of a formerly coherent biofilm. The outgrowths and ball-shaped ends of filaments were interpreted by Zhmur (2003) as spherical swellings of the filament sheaths produced by degassing. However, their size and transition to botryoidal and dented structures (Fig. 5) is more consistent with an interpretation as a primary feature, because we don't see an easy way to produce these features by fossilization. In addition, the cross sections (Fig. 7) of these structures with regular outline of e.g. the distribution of fluorescence and the mappings (Fig. 10) also indicate a primary feature. In contrast, the more irregular, ridge-like features (Fig. 3d), covered with platy clay minerals such as kaolinite (Figs. 3, 6g,h), seem to represent strongly modified, original segmentation of the filaments during the fossilization process.

Many, but not all of the broken filaments show a central channel (Fig. 6), visible also in BSE images of embedded filaments in cross sections, and it is the question if this is a primary or a secondary fossilization feature. In small nanometer-scale channels, the ratio of the solid outer part to channel is $\approx$ 10:1 (in cross section, see Fig. 6a,c), and together with the observation that not all filaments have this channel, it might be interpreted as a shrinking phenomenon. However, in µm-sized channels the ratio goes down to $\approx$ 1:1 (Fig. 6f,h), and such a high loss of material during degassing seems unlikely. Furthermore, the six-sided outline, seen in small and large channels, cannot be explained by shrinking. There is no reason why a cylindrical body during shrinking should open a central channel with a regular outline.

In order to describe the infiltration process for the fossilization and the responsible fluid phase, it is important to note that kerite occurs not only with the well-preserved morphology described above, but also in patches of highly degraded OM, as shown in the previous description of a breccia from these pegmatites (Franz et al., 2017). This OM is not only highly oxygenated (with

518   up to 40 atom% of O), but is also enriched in F ($\leq$ 1.7 atom%), Zr ($\leq$ 7 atom%), Sc ($\leq$ 0.8

519   atom%), Y ($\leq$ 2.7 atom%), and REE (sum $\leq$ 0.35 atom%), elements that were most probably

520   derived from the pegmatitic environment.

521   What is striking in all observations is the close connection between kerite and fluorite, which

522   was also described by Zhmur (2003). The whole occurrence in the granitic pegmatites with a

523   large amount of topaz in the chambers (Lyckberg et al., 2019, report that a single pegmatite,

524   no. 464, had produced 6 tons topaz in mining) points to a high concentration of F in the late-

525   magmatic to hydrothermal fluids. In addition, we observed F-rich muscovite during the

526   formation of the breccia (Franz et al., 2017) and this also points to the importance of F-activity.

527   This fluid likely carried a high amount of silica as SiF_4 (plus other components, such as Al,

528   alkalies, Ca, Mg, and Fe).

529   For the fossilization process we assume that this fluid was able to react with kerite in a depth

530   of 1-2 µm (Figs. 7-10). Gorlenko et al. (2000) and Zhmur (2003) described the outer part of the

531   filaments as a former sheath of the microorganisms. We interpret this rim area as a former thin

532   coating of biofilm that was probably very sensitive in a first stage of Si-Al-infiltration, with Ca-

533   infiltration slightly deeper into kerite. The small mineralized structures on the surface of

534   filaments (Fig. 3c) resemble what Gorlenko et al. (2000) interpreted as membrane leaflets.

535   **3.2 Environment of fossilization**

536   The geological situation for the fossilization is summarized in Figure 15. We assume that

537   fossilization must have occurred during a hydrothermal event within a fluid that carried enough

538   Si, Al, F, and Ca to react with the kerite degradation products in nano-environments. The

539   Korosten pluton intruded into continental crust, and the geological situation indicates a long-

540   living plutonic-volcanic activity (Shumlyanskyy et al., 2021), likely with near-surface geyser

541   systems. The crystallization of the pegmatites and formation of the chambers occurred in a

542   depth of 2 to 2.5 km (Lukashev, 1976, Kalyuzhnyi et al., 1971; Voznyak et al., 2007). The

543   miarolitic cavities of the granite, possibly with periodical influx of hydrothermal waters,

544   provided the space for a continental deep biosphere, consisting probably of anaerobic,

545   thermophilic, and acidophilic microbial species. Methanogenic microbes (indicated by C and

546   N stable isotopes; Franz et al., 2017) might have been an important part of such a cryptic

547   endolithic micro-ecosystem in a continental, terrestrial environment.
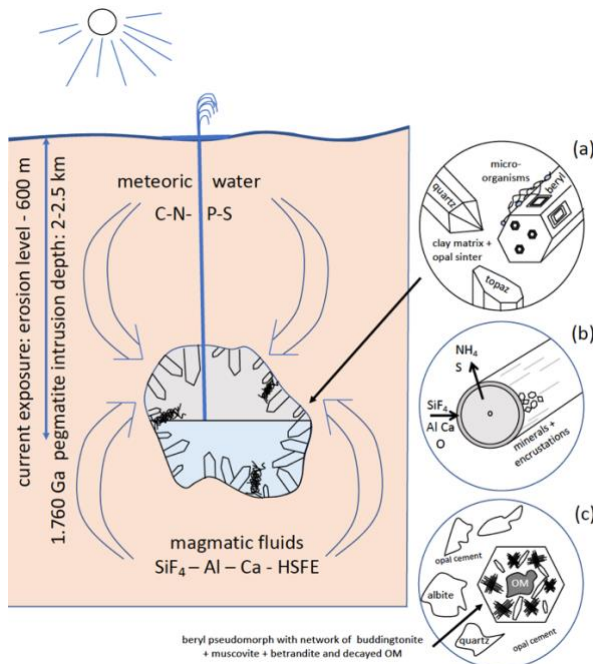
548

549   **Figure 15: Schematic illustration of the geological environment of pegmatites of the**
550   **Korosten pluton, Ukraine, with m-sized miarolitic chambers and a near-surface geyser**
551   **system. The chambers provided the space for an endolithic micro-ecosystem, which**
552   **consists (a) of organisms with three morphologically different types (filamentous, flaky,**
553   **and rare spherical), attached to the pegmatitic minerals, also in etch pits of beryl. (b)**
554   **Fossilization occurs due to influx of hydrothermal fluids, carrying SiF_4 and starts with a**
555   **µm-thin layer of Al-Si enrichment, which develops into clay minerals, feldspar, and finally**
556   **into encrustations. (c) Strongly degraded OM is found also in breccias, formed during**
557   **collapse of some chambers, providing NH_4 for the formation of buddingtonite, together**
558   **with muscovite and bertrandite, in pseudomorphs after beryl.**

559

560   The flaky kerite, also visible as thin films in cross section, point to the participation of biofilms

561   in this ecosystem, which might have developed as soon as the temperatures in the miarolitic

562   chambers were sufficiently low for organisms to live in this environment. The essential

563   components for the organisms - C, N, S, P - or the microorganisms themselves were transported

with meteoric water from the surface to the chambers. Alternatively, the components for the organisms might have been transported from the metamorphic country rocks of the Korosten pluton into the chambers via hydrothermal convection cells (e.g. Bobos and Williams, 2017, who described NH_4-transport for tobelite formation in a sedimentary basin).

Some of the miarolitic cavities collapsed and produced a breccia, which also contains degraded OM and black opal with inclusion of carbohydrates (Franz et al., 2017). Chambers, which did not collapse, must have been sealed. They contained a large amount of gas under high pressure, and the sealing preserved the gas from escape. Lyckberg et al. (2019) reported that old log books of the mining activities in Volyn describe an event in 1955, when at a depth of 600 m drilling penetrated a gas-filled cavity, and as a consequence the entire drill steel shot out of the hole and toppled the drill tower. It took more than 30 min, before the highly pressurized gas slowed down. That a large amount of gas must have been produced during decay of the OM is also indicated by the fluid-solid equilibria between NH_4^+ and K^+, responsible for the buddingtonite formation. It is known from experimental data that for the transformation of K-feldspar into buddingtonite, X_{NH4} in the fluid must be very high (Pöter et al., 2004).

Laser-ablation dating with the $^{39}Ar/^{40}Ar$ method of the muscovite from the breccia yielded an age of 1491±9 Ma (MSWD 0.98), interpreted as the age of the hydrothermal breccia formation (Franz et al., 2021). Analyses of buddingtonite yielded an age range from 383±12 Ma to 563±14 Ma, and the oldest age of 563 Ma is interpreted as a minimum age, because of probable Ar-loss of the very fine-grained buddingtonite crystals. This minimum age is in the same range as the results of our attempt to date the fossils directly with Pb-Pb-dating (Fig. 14). The maximum age is given by the intrusion age of the pegmatites, 1760±3 Ma (Fig. 1; Shumlyanksyy et al., 2021). The intrusion depth of 2 to 2.5 km might have been the depth for the microbial community, but there is a significant time lag between pegmatite formation (1.76 Ga) and the formation of the breccia (c. 1.49 Ga) during which exhumation could have occurred.

589   Silicification of microbial organisms is typical for geyser systems, as shown by many recent

590   analogues, e.g. for Yellowstone, USA (Cady and Farmer, 1996), Waiotapu, New Zealand

591   (Handley et al., 2008) and others (see references in Alleon et al, 2016). Consequently, a number

592   of experimental studies on silicification of microorganisms including the processes of silica

593   polymerization and precipitation in the presence of microorganisms was undertaken, starting

594   with the earliest work by Oehler (1976). Experimental silicification of archaea (Orange et al.,

595   2009) has shown that the outer surface layer of these organisms is the site for incipient

596   silicification, and the ubiquity of biofilms on surfaces in hot-springs (e.g. Cady and Farmer,

597   1996; Handley et al., 2008; Kremer et al., 2012) and other environments (Bortnikov et al., 2012)

598   indicates potential presence of biofilms also in the Precambrian at the subvolcanic geyser

599   system in the Korosten pluton. Extracellular polymeric substances play an important role in

600   silicification and fossilization as shown by many authors (see references above, and therein),

601   and fossilization of biofilms occurs very rapidly (Rozanov, 2003). After silicification of

602   extracellular polymeric substances, clay minerals developed on the surface of the fossils from

603   Volyn. This phenomenon was also observed in experimental studies (Urrutia and Beveridge,

604   1994) and in natural environments (Kremer et al., 2012; Bortnikov et al., 2012).

605   The formation of the 1-2 µm thick layer of Si-Al infiltration and development of encrustations

606   of Al-silicates was essential for the excellent preservation of the morphology of the

607   microfossils. The fossilization of organisms without skeletal parts requires special conditions,

608   which prevent autolysis. In fossilization experiments of crustacean eggs with phosphoric acid,

609   Hippler et al. (2012) pointed out that rapid heating before treatment with phosphoric acid was

610   essential for perfect preservation of the morphology of OM. This treatment denaturized the

611   proteins of the crustacean eggs, creating a stable template for mineralization, which occurred

612   rapidly within one to two weeks. We suspect a similar process for the silicification process at

613   the Volyn locality. Anoxic conditions in the deep biosphere prevented early autolysis of the

614   organisms, then shock heating might have occurred due to influx of hot hydrothermal waters

into the miarolitic caves, carrying SiF_4 together with Al, Ca, and other elements, producing

rapid infiltration of Si, Al, and Ca into the outer surface layer of the organisms, including

precipitation of opal (Fig. 4f). The early envelope of silicification minimizes the molecular

degradation of the fossils, as also shown experimentally by Alleon et al. (2016). Further heating

(without deformation) after formation of the Si-Al enriched outer rim enhanced the decay, but

did not destroy the morphology. Kremer at al. (2012) pointed out that the morphology of

calcified cyanobacteria was destroyed, whereas silicification, when rapid, helps to preserve

their morphological details (e.g., Bartley, 1996; Manning-Berg et al., 2019, and refs therein).

That fossilization of bacterial organisms is a rapid process has also been postulated by Rozanov

(2003). Raff et al. (2008) demonstrated experimentally that under anoxic conditions (preventing

autolysis) rapid formation of bacterially induced biofilms on the surface of organisms provided

the site for early mineralization with Ca-minerals. These biofilm bacteria induce a catalyzing

process for rapid fine-grained mineralization, which was also postulated by Briggs (2003).

Extracellular polymeric substances are known to provoke diagenetic mineralization, possibly

as the result of liberation of adsorbed cations during degradation (Arp et al., 1999; Dupraz and

Visscher, 2005; Altermann et al., 2006). Notably, most of the cases described in the literature

and quoted above deal with marine environments, whereas the case reported here deals with a

Precambrian continental, subsurface environment. Only in the continental environment fluids

rich in F are present; in the oceanic environment granites are much less abundant than mafic

rocks and they commonly lack F-enriched pegmatites.

Extracellular biosilicification capability of bacteria and archaea in geothermal environments

with transformation of soluble $Si(OH)_4$ into nano-scale SiO_2 precipitates on the surface has

recently been emphasized by Ikeda (2021). Bacteria, such as *Thermus thermophilus* (Iwai et

al., 2010), can form siliceous deposits from supersaturated solutions in biofilms on the outer

surface layer of the cell envelope.

640   Zhmur (2003), based on the data by Gorlenko et al. (2000) and by comparison with other

641   occurrences in igneous rocks and in recent geyser environments, proposed a hydrothermal

642   origin of cyanobacteria and microbial bio-mats in geyser ponds for the Volyn occurrence. The

643   fossilization occurred in situ in zones of silica precipitation, forming sealed cup-like structures.

644   The floating cyanobacterial mat was buried in the self-sealed biogenic-geyser structure that was

645   formed at the hydrothermal discharge site, and collapse of these structures produced the breccia,

646   observed at the Volyn deposit. This model implies that the fossils were transported downward

647   with the geyser water to the chambers, because photosynthesizing cyanobacteria must have

648   lived at the surface. This is not consistent with our observations, which show that the filaments,

649   together with irregular and spherical kerite grew onto and into the etch pits of beryl (Fig. 3a).

650   If transport had occurred, this would have probably destroyed the delicate filaments, producing

651   a mat-like OM, such as described by Zhmur (2003).

652

4 Concluding remarks

654   The pegmatitic Volyn kerite occurrence is probably one of the localities world-wide with the

655   best preserved Precambrian microfossils. Common occurrences of (Precambrian) fossils are in

656   sedimentary rocks, especially in chert, but there is growing evidence of OM in the pore space

657   of igneous rocks (Ivarsson et al., 2020). Several factors have contributed to the micro-

658   taphonomical process to preserve the Volyn fossils as part of an endolithic micro-ecosystem.

659   First, the chambers in the pegmatites provided an exceptionally large 'pore' space. Secondly,

660   water was present in such an environment, necessary for life, although this space was not

661   necessarily completely water-filled, but possibly a cavity with temporary changes in the water

662   level. Transport of Si was likely enhanced by F, present in this pegmatitic, granitic environment.

663   OM would have decayed, when O was available, hence silicification of the outer parts of the

664   kerite fossils implies rapid reaction with Si and shielding for access of O. This environment in

the deep biosphere was similar to geyser systems, which are known to be sites of preferred microbial growth. The microorganisms contribute to the microstructural development of geyserites by providing a favored substrate for opaline silica precipitation, and encrustation and degradation of microorganisms is the dominant mode of fossilization at the high temperature end of the geyser system (Cady and Farmer, 1996).

There is growing awareness of the importance of life in the deep igneous biosphere especially in the record of early life, the most important reservoir of biomass in the Precambrian (Ivarsson et al. 2020). The presence of F-rich hydrothermal waters in the late stage of granitic, subvolcanic plutons might be a common scenario for preservation of microorganisms, without the later influence of deformation and metamorphism, such as in chert, where most of the studies of Precambrian fossils has been undertaken. Granitic rocks might be sites for the very early diagenetic emplacement of silica, leading to 3D preservation of non-biomineralizing fossils, the "Bitter Springs-type preservation" (Butterfield, 2003). The search for indications for early life, and its evolution during the Precambrian has concentrated mainly on submarine hydrothermal vents (e.g. Dodd et al., 2017), but it should be extended also to terrestrial environments.

Acknowledgements

We thank A. Schreiber for preparation of FIB foils and D. Hippler for comments on an earlier version, two anonymous reviewers for their careful and helpful reviews, and Tina Treude for editorial handling.

Author contributions: GF (concept, writing), PL (sampling, reviewing), VC (sampling), VK (sampling), H-MS (reviewing, reflected light microscopy), NM (pyrolysis), RW (TEM), JG (U-Th-Pb), UG (SEM), JN (EMPA)

689 **Funding:** VK acknowledges financial support from Akademisches Auslandsamt Technische
690 Universität Berlin.

691

References

693 Alleon, J., Bernard, S., Le Guillou, C., Daval, D., Skouri-Panet, F., Pont, S., Delbes., and
694 Robert, F.: Early entombment within silica minimizes the molecular degradation of
695 microorganisms during advanced diagenesis, Chem. Geol., 437, 98-108, 2016.

696 Altermann, W., Kazmierczak, J., Oren, A., and Wright, D. T.: Cyanobacterial calcification and
697 its rock-building potential during 3.5 billion years of Earth history, Geobiology, 4,147–166,
698 2006.

699 Arp, G., Reimer, A., Reitner, J.: Calcification in cyanobacterial biofilms of alkaline salt lakes,
700 Eur. J. Phycol., 34, 393–403, 1999.

701 Bartley, J. K.: Actualistic taphonomy of cyanobacteria: implications for the Precambrian fossil
702 record, Palaios, 571-586, 1996.

703 Burnham, A.K., and Sweeney, J.J.: A chemical kinetic model of vitrinite maturation and
704 reflectance, Geochim. Cosmochim. Acta, 53, 2649-2657, 1989.

705 Butterfield, N. J.: Exceptional fossil preservation and the Cambrian explosion, Integr. Compar.
706 Biol., 43, 166-177, 2003.

707 Bobos, I., and Williams, L. B.: Boron, lithium and nitrogen isotope geochemistry of NH_4-illite
708 clays in the fossil hydrothermal system of Harghita Bãi, East Carpathians, Romania, Chem.
709 Geol., 473, 22-39, 2017.

710 Bortnikov, N. S., Novikov, V. M., Soboleva, S. V., Savko, A. D., Boeva, N. M., Zhegallo, E.
711 A., and Bushueva, E. B.: The role of organic matter in the formation of fireproof clay of the
712 Latnenskoe Deposit, Dokl. Earth Sci., 444, No. 1, 634-639, 2012.

713 Briggs, D. E. G.: The role of decay and mineralization in the preservation of soft-bodied fossils,
714 Annu. Rev. Earth Planet. Sci., 31, 275–301, 2003.

715 Cady, S. L., and Farmer, J. D.: Fossilization processes in siliceous thermal springs: trends in
716 preservation along thermal gradients, Evolution of hydrothermal ecosystems on Earth and
717 Mars? Chichester (Ciba Foundation Symposium), Wiley, 202, 150-173, 1996.

718 Dodd, M. S., Papineau, D., Grenne, T., Slack, J. F., Rittner, M., Pirajno, F., O'Neill, J., and
719 Little, C. T.: Evidence for early life in Earth's oldest hydrothermal vent precipitates, Nature,
720 543(7643), 60-64, 2017.

721 Dormans H.N.M., Huntgens F.J. and van Krevelen D.W.: Chemical structure and properties
722 of coal: 20. Composition of the individual macerals, Fuel 36, 321-339, 1957.

723 Dupraz, C., Visscher, P. T.: Microbial lithification in marine stromatolites and hypersaline
724 mats, Trends Microbiol. 13, 429–438, 2005.

725 England, W., and Mackenzie, A.: Some aspects of the organic geochemistry of petroleum
726 fluids, Geolog. Rundschau 78, 291-30, 1989.

727 Franz, G., V. Khomenko, Vishnyevskyy, A., Wirth, R., Struck, U., Nissen, J., Gernert, U., and
728 Rocholl, A.: Biologically mediated crystallization of buddingtonite in the Paleoproterozoic:
729 Organic-igneous interactions from the Volyn pegmatite, Ukraine, Amer. Mineral., 10, 2119-
730 2135, 2017.

731 Franz, G., Sudo, M., Khomenko, V. (in revision): $^{40}Ar/^{39}Ar$ dating of a hydrothermal pegmatitic
732 buddingtonite-muscovite assemblage from Volyn, Ukraine, Eur. J. Mineral.

733 Ginzburg, A.I., Bulgakov, V.S., Vasilishin, I.S., Luk'yanova, V.T., Solntseva, L.S., Urmenova,
734 A.M., and Uspenskaya, V.A.: Kerite from pegmatites of Volyn, Dokl. Akad. Nauk SSSR, 292,
735 188–191, 1987, (in Russian).

736 Gorlenko, V.M., Zhmur, S.I., Duda, V.I., Osipov, G.A., Suzina, N.E., and Dmitriev, V. V.: Fine
737 structure of fossilized bacteria in Volyn kerite, Origin of Life and Evolution of the Biosphere,
738 30, 567–577, 2000.

739 Handley, K. M., Turner, S. J., Campbell, K. A., and Mountain, B. W.: Silicifying biofilm
740 exopolymers on a hot-spring microstromatolite: templating nanometer-thick laminae,
741 Astrobiol., 8(4), 747-770, 2008.

742 Hippler, D., Hu, N., Steiner, M., Scholtz, G., and Franz, G.: Experimental mineralization of
743 crustacean eggs: new implications for the fossilization of Precambrian–Cambrian embryos,
744 Biogeosci., 9(5), 1765-1775, 2012.

745 Horsfield, B.: Practical criteria for classifying kerogens: Some observations from pyrolysis-gas
746 chromatography, Geochim. Cosmochim. Acta, 53, 891-901, 1989.

747 Ikeda, T.: Bacterial biosilicification: a new insight into the global silicon cycle, Biosci.,
748 Biotechn., Biochem., 85, 6, 1324-1331, 2021.

749 Ivanovich, P. V., and Alekseevich, D. S.: Mineralogy of the Volynian chamber pegmatites,
750 EKOST Association, Mineral. Almanac, 12, 128 p, Moscow, 2007.

751 Ivarsson, M., Drake, H., Neubeck, A., Sallstedt, T., Bengtson, S., Roberts, N. M. W., and
752 Rasmussen, B.: The fossil record of igneous rocks, Earth Sci. Rev., 210, 2020.

753 Iwai, S., Doi, K., Fujino, Y., Nakazono, T., Fukuda, K., Motomura, Y., and Ogata, S.: Silica
754 deposition and phenotypic changes to *Thermus thermophilus* cultivated in the presence of
755 supersaturated silicia, The ISME J. 4, 809–816, 2021.

756 Kalyuzhnyi V. A., Voznyak, D. K., Gigashvili, G. M.: Mineral-forming fluids and mineral
757 paragenesis of chamber pegmatites of Ukraine, Kyiv: Naukova Dumka, 216 pp., 1971 (in
758 Ukrainian).

759 Kremer, B., Kazmierczak, J., Lukomska-Kowalczyk, M., and Kempe, S.: Calcification and
760 silicification: fossilization potential of cyanobacteria from stromatolites of Niuafo'ou's Caldera
761 Lakes (Tonga) and implications for the early fossil record, Astrobiol. 12(6), 535-548, 2012.

762 Larter, S.R.: Application of analytical pyrolysis techniques to kerogen characterisation and
763 fossil fuel exploration/exploitation, in: Voorhees, K. (Ed.): Analytical pyrolysis, methods and
764 applications. Butterworth, London, pp. 212-275, 1984.

765 Lukashev, A. N.: Depth of pegmatite formation, Moscow, Nedra, 152 pp., 1976, (in Russian).

766 Lu'kyanova, V. T., Lobzova, R. V., and Popov, V. T.: Filaceous kerite in pegmatites of Volyn,
767 Izvest. Ross. Akad. Nauk Ser. Geologicheskaya, 5, 102–118, 1992 (in Russian).

768 Lyckberg, P., Chernousenko, V., and Wilson, W. E.: Famous mineral localities: Volodarsk-
769 Volynski, Zhitomir Oblast, Ukraine, The Mineral. Record 40, 473-506, 2009.

770 Lyckberg, P., Chournousenko, V., and Chournousenko, O.: Giant heliodor and topaz pockets
771 of the Volodarsk chamber pegmatites, Korosten pluton, Ukraine, 36th Intern. Gemm. Conf..
772 Nantes, France, Abstr. vol., 78-83, 2019.

773 Mahlstedt, N., di Primio, R., and Horsfield, B.: On the shale gas potential of the Georgina Basin,
774 Record 2014 Geoscience Australia, Canberra, 2014.

Mahlstedt, N., di Primio, R., Horsfield, B., and Boreham, C.J.: Multi-component kinetics and late gas potential of selected Cooper Basin source rocks, Record 2015/19 Geosci. Australia, Canberra, pp. 199. http://dx.doi.org/110.11636/Record.12015.11019, 2015.

Manning-Berg, A. R., Wood, R. S., Williford, K. H., Czaja, A. D., and Kah, L. C.: The taphonomy of proterozoic microbial mats and implications for early diagenetic silicification, Geosci., 9, 40, 2019.

Oberlin A., Boulmier J.L., and Durand B.: Electron microscope investigation of the structure of naturally and artificially metamorphosed kerogen, Geochim. Cosmochim. Acta, 38, 647-650, 1974.

Oehler, J.H.: Experimental studies in Precambrian paleontology: structural and chemical changes in blue-green algae during simulated fossilization in synthetic chert, Geol. Soc. Am. Bull. 87 (1), 117–129, 1976.

Orange, F., Westall, F., Disnar, J. R., Prieur, D., Bienvenu, N., Le Romancer, M., and Défarge, C.: Experimental silicification of the extremophilic Archaea Pyrococcus abyssi and Methanocaldococcus jannaschii: applications in the search for evidence of life in early Earth and extraterrestrial rocks, Geobiol., 7(4), 403-418, 2009.

Pöter, B., Gottschalk, M., and Heinrich, W.: Experimental determination of ammonium partitioning among muscovite, K-feldspar, and aqueous chloride solutions, Lithos, 74, 67–90, 2004.

Poetz, S., Horsfield, B., and Wilkes, H.: Maturity-driven generation and transformation of acidic compounds in the organic-rich Posidonia Shale as revealed by electrospray ionization Fourier transform ion cyclotron resonance mass spectrometry, Energy Fuels, 28, 4877–4888, 2014.

Quigley, T. M., and Mackenzie, A. S.: The temperatures of oil and gas formation in the sub-surface, Nature, 333, 549-552, 1988.

Radke M., Horsfield B., Littke R. and Rullkötter, J.: Maturation and petroleum generation. In: Welte, D.H., Horsfield, B., Baker, D.R. (Eds.), Petroleum and Basin Evolution: Insights from Petroleum Geochemistry, Geology and Basin Modeling. Springer Berlin Heidelberg, Berlin, Heidelberg, 169–229, 1997.

Raff, E. C., Schollaert, K. L., Nelson, D. E., Donoghue, P. C., Thomas, C. W., Turner, F. R., and Raff, R. A.: Embryo fossilization is a biological process mediated by microbial biofilms, Proc. Nat. Acad. Sci., 105(49), 19360-19365, 2008.

Rozanov, A. Yu.: Fossil bacteria, sedimentogenesis, and the early biospheric evolution, Paleontol. Zh., No. 6, 41–49, 2003, [Paleontol. J. 37 (6), 600–608 (2003)].

Shumlyanskyy, L., Belousoca, E., and Petrenko, O.: Geochemistry of zircons from basic rocks of the Korosten anorthosite-mangerite-charnockite-granite complex, northwestern region of the Ukranian Shield, Mineral. Petrol., 111(4), 459-466, 2017.

Shumlyanskyy, L., Franz, G., Glynn, S., Mytrokhyn, O., Voznyak, D., and Bilan O.: Geochronology of granites of the western part of the Korosten AMCG complex (Ukrainian Shield): implications for the emplacement history and origin of miarolitic pegmatites, Eur. J. Min., 33, 703-716, 2021.

Sinninghe Damsté, J.S., Eglinton, T.I., De Leeuw, and J.W., Schenck, P.A.: Organic sulphur in macromolecular sedimentary organic matter: I. Structure and origin of sulphur-containing moieties in kerogen, asphaltenes and coal as revealed by flash pyrolysis, Geochim. Cosmochim. Acta, 53, 873-889, 1989.

820 Tahán, J. E., Granadillo, V. A., Sánchez, J. M., Cubillán, H. S., and Romero, R. A.:
821 Mineralization of biological materials prior to determination of total mercury by cold vapour
822 atomic absorption spectrometry, J. Anal. Atomic Spec., 8(7), 1005-1010, 1993.

823 Urrutia, M. M., and Beveridge, T. J.: Formation of fine-grained metal and silicate precipitates
824 on a bacterial surface (Bacillus subtilis), Chem. Geol., 116(3-4), 261-280, 1994.

825 Tissot, B.P., and Welte, D.H.: Petroleum formation and occurrence, 2nd ed. Springer-Verlag,
826 Berlin, 1984.

827 Vermeesch, P.: IsoplotR: a free and open toolbox for geochronology, Geosci. Front., 9, 1479-
828 1493, 2018 doi: 10.1016/j.gsf.2018.04.001.

829 Voznyak, D.K., Khomenko, V.M., Franz, G., and Wiedenbeck, M. Physico-chemical
830 conditions of the late stage of Volyn pegmatite evolution: Fluid inclusions in beryl studied by
831 thermobarometry and IR-spectroscopy methods, Mineral. J. (Ukraine), 34, 26–38, 2012 (in
832 Ukrainian).

833 Wirth, R.: Focused Ion Beam (FIB): a novel technology for advanced application of micro-and
834 nanoanalysis in geosciences and applied mineralogy, Eur. J. Mineral., 16, 863–876, 2004.

835 Wirth, R.: Focused ion beam (FIB) combined with SEM and TEM: Advanced analytical tools
836 for studies of chemical composition, microstructure and crystal structure in geomaterials on a
837 nanometre scale, Chem. Geol., 261, 217-229, 2009.

838 Zhmur, S. I.: Origin of Cambrian fibrous kerites of the Volyn region, Lithol. Mineral Resour.,
839 38, 55-73, 2003.